Scanning thermal microscopy with heat conductive nanowire probes

Maria Timofeeva[a, d*], Alexey Bolshakov[a], Peter D. Tovee[b], Dagou A. Zeze[c, d], Vladimir G. Dubrovskii[a, d] and Oleg V. Kolosov[b*]

[a]*Laboratory of Physics of Nanostructures, Nanotechnology Centre, Saint-Petersburg Physics and Technology Centre for Research and Education of Russian Academy of Sciences, 8, bld. 3 Khlopina, St. Petersburg, 194021, Russia; timofeeva_m@list.ru*
[b]*Physics Department, Lancaster University, Lancaster, LA1 4YB, UK; o.kolosov@lancaster.ac.uk*
[c]*School of Engineering and Computing Sciences, Durham University, Durham DH1 3LE, United Kingdom*
[d]*Saint-Petersburg National Research University of Information Technologies, Mechanics and Optics (ITMO), Kronverkskiy pr. 49, 197101 St. Petersburg, Russia*

*corresponding author: *timofeeva_m@list.ru*

Abstract

Scanning thermal microscopy (SThM), which enables measurement of thermal transport and temperature distribution in devices and materials with nanoscale resolution is rapidly becoming a key approach in resolving heat dissipation problems in modern processors and assisting development of new thermoelectric materials. In SThM, the self-heating thermal sensor contacts the sample allowing studying of the temperature distribution and heat transport in nanoscaled materials and devices. The main factors that limit the resolution and sensitivities of SThM measurements are the low efficiency of thermal coupling and the lateral dimensions of the probed area of the surface studied. The thermal conductivity of the sample plays a key role in the sensitivity of SThM measurements. During the SThM measurements of the areas with higher thermal conductivity the heat flux via SThM probe is increased compared to the areas with lower thermal conductivity. For optimal SThM measurements of interfaces between low and high thermal conductivity materials, well defined nanoscale probes with high thermal conductivity at the probe apex are required to achieve a higher quality of the probe-sample thermal contact while preserving the lateral resolution of the system.

In this paper, we consider a SThM approach that can help address these complex problems by using high thermal conductivity nanowires (NW) attached to a tip apex.

We propose analytical models of such NW-SThM probes and analyse the influence of the contact resistance between the SThM probe and the sample studied. The latter becomes particularly important when both tip and sample surface have high thermal conductivities.

These models were complemented by finite element analysis simulations and experimental tests using prototype probe where a multiwall carbon nanotube (MWCNT) is exploited as an excellent example of a high thermal conductivity NW. These results elucidate critical relationships between the performance of the SThM probe on one hand and thermal conductivity, geometry of the probe and its components on the other. As such, they provide a pathway for optimizing current SThM for nanothermal studies of high thermal conductivity materials. Comparison between experimental and modelling results allows us to provide direct estimates of the contact thermal resistances for various interfaces such as MWCNT-Al ($5\times10^{-9} \pm 1\times10^{-9}$ K m^2 W^{-1}), Si_3N_4-Al ($6\times10^{-8} \pm 2.5\times10^{-8}$ K m^2 W^{-1}) and Si_3N_4–graphene (~10^{-8} K m^2 W^{-1}). It was also demonstrated that the contact between the MWCNT probe and Al is relatively perfect, with a minimal contact resistance. In contrast, the thermal resistance between a standard Si_3N_4 SThM probe and Al is an order of magnitude higher than reported in the literature, suggesting that the contact between these materials may have a multi-asperity nature that can significantly degrade the contact resistance.

Keywords: scanning thermal microscopy; SThM; nanoscale imaging; thermal conductivity; contact thermal resistance; carbon nanotubes; nanowires.

1. Introduction

Modern materials science and technology is increasingly devoted to the control of matter on the nanoscale, with local thermal properties playing a major role in the diverse materials used in renewable energy generation (thermoelectrics, photovoltaics), structural composites and in optical and electronic devices [1-6]. In semiconductor processors, the inability to dissipate increasing power density leads to the failure of Moore's law due to nanoscale thermal management problems [7-9]. Tools able to perform thermal measurements of solid state materials on the nanoscale are needed to address these problems. Unfortunately, most thermal measurement systems are based on optical methods, such as IR thermal emission, Raman spectroscopy or photoreflectance with the spatial resolution limited in the best case to 500 nm or greater [10-12]. A promising technique for nanoscale thermal measurements is Scanning Thermal Microscopy (SThM) [13-19]. While showing good performance in studies of polymeric and organic materials, SThM has a limited ability to study high thermal conductivity materials such as those frequently used in the semiconductor industry, e.g. heatsinks in integrating circuits and thermoelectric assemblies or optical devices. The main limiting factors for conventional SThM are briefly summarized: (i) SThM spatial resolution, which is in the range of a few tens of nanometres, remains well below most other scanning

probe microscopy (SPM) approaches: (ii) SThM has low sensitivity to thermal properties of materials of high thermal conductance such as metals and single crystal semiconductors that are indispensable for the semiconductor industry and nanotechnology; (iii) finally the performance of SThM is significantly affected by the unstable and weak thermal contact between the heat sensor and the specimen studied.

One of the possible solutions proposed elsewhere [4, 5, 20, 21] suggests to use a high thermal conductivity and nanometre scale cross-section probe at the apex of the tip (e.g. nanowire (NW) or multiwall carbon nanotube (MWCNT), a particular example of NW) to act as a nanometre scale thermal link between the sensor and the sample [21, 22]. The first experimental tests [5, 22] showed the high potential of such an approach. This paper focuses on the understanding of the physical principles underlying the operating envelope of such high performance SThM probes. It also correlates the geometry of the probe and the characteristics of the materials used. An analytical thermal model was developed considering all probe components to define overall SThM sensitivity and spatial resolution. The validity of the model was tested by comparing finite elements analysis to experimental measurements. This allowed us to propose the optimal geometry and materials for such a high performance probe including semiconductor and MWCNT based thermal nanowires that may add new functionalities to SThM measurements. The thermal sensitivity of the NW-probe was compared with the experimental results obtained using MWCNT-probe. We then analyse future directions to optimize the performance of such SThM probes in air and vacuum environments. For simplicity, the term "NW" is used throughout the paper for both semiconducting and MWCNT nanowires.

2. Theory and simulation.

2.1 Analytical model of the SThM probe

Fig. 1 shows a scanning electron microscope (SEM) image of the widely used SThM probes (Kelvin Nanotechnologies) [18, 19] with a Si_3N_4 cantilever and Pd/NiCr heater. This SThM cantilever has a Si_3N_4 cantilever base with Au pads, that are highly conductive both electrically and thermally [23] (Fig. 1a). The high resistance Pd/NiCr heating resistor acts as a thermal sensor and is positioned on the triangular part of the cantilever (Fig. 1b) and the probe apex zone that is either in direct thermal contact with the sample or via a NW attached[4, 22] (Fig. 1c).

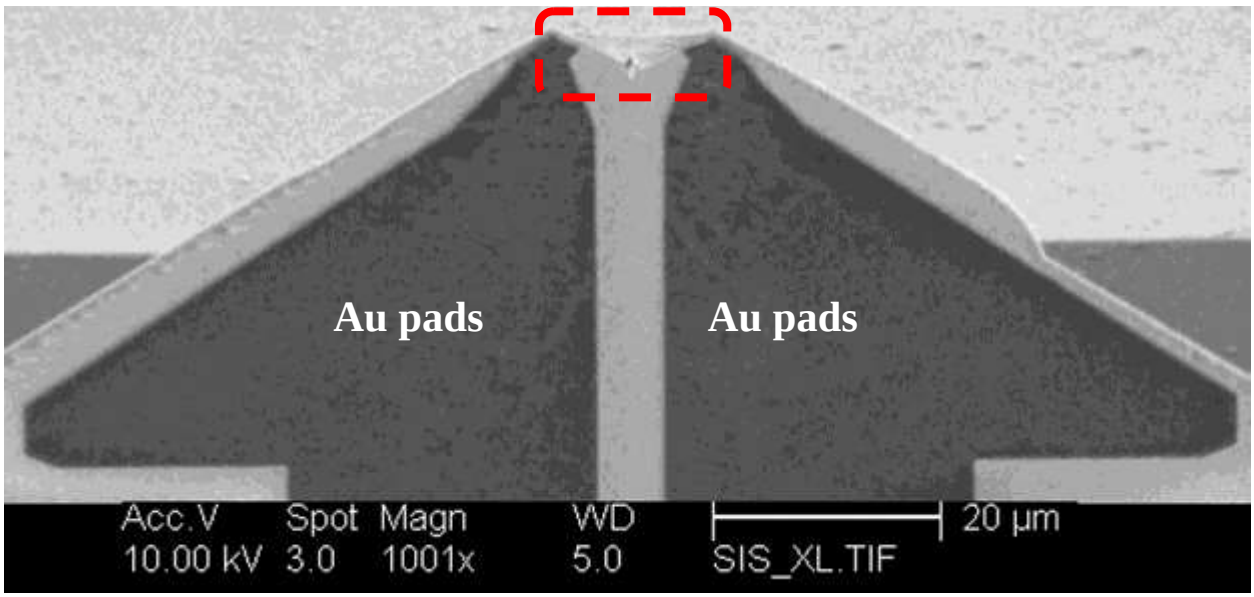

(a)

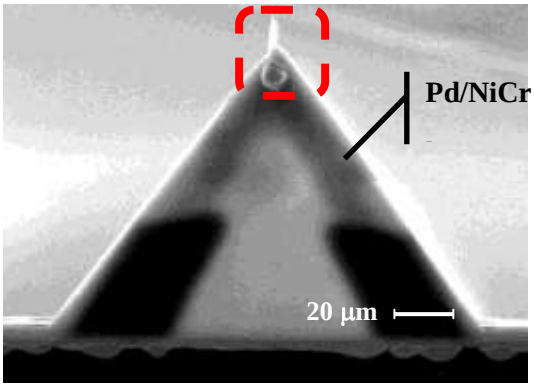

(b)

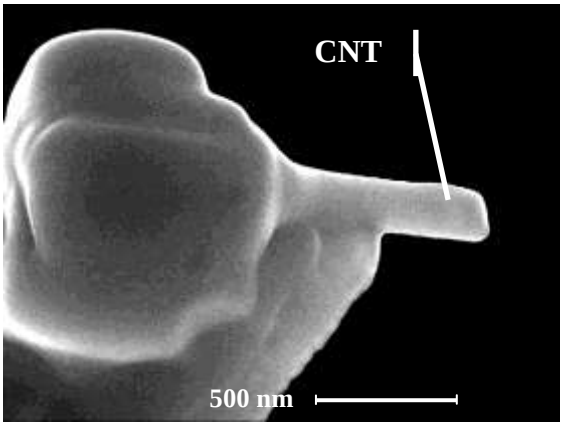

(c)

Fig. 1. SEM image of the SThM cantilever, (a) SThM cantilever base with Au pads, (b) high resistance Pd/NiCr heating resistor that also acts as a thermal sensor that is positioned on the triangular part of the cantilever (scale 2µm), (c) attached NW (scale 500 nm).

It was demonstrated elsewhere [4, 6, 24-26] that the thermal properties of the tip apex have a major impact on the performance of the SThM probe. Therefore, this study focuses on the apex of the SThM probe (dashed square in the Fig. 1b and Fig. 1c) and the contact of the probe with the sample studied. The equivalent thermal resistance of the SThM probe is schematically presented in Fig. 2, in line with previously reported models [4, 23].

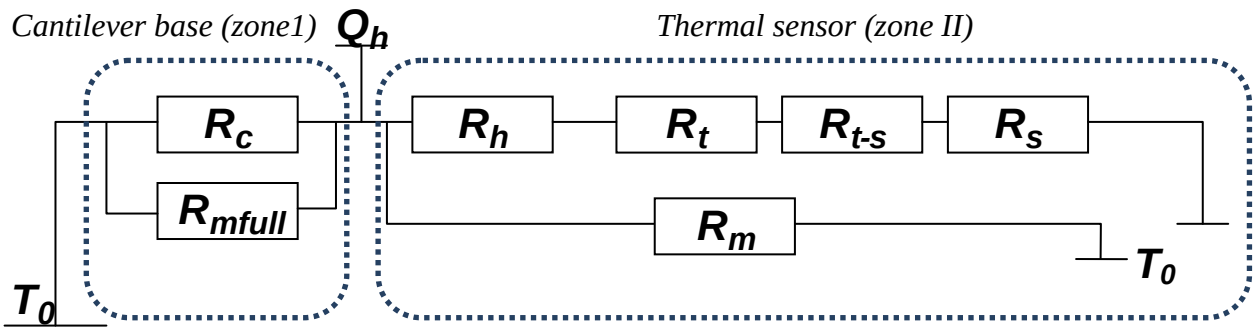

Fig. 2 Equivalent thermal resistance diagram of the SThM system, depicting the properties of the cantilever and the probe (including NW), probe-sample interface, sample and surrounding media.

Here R_c is the thermal resistance of the cantilever base, R_{mfull} is the thermal resistance of the heat flow to the media surrounding the cantilever (excluding the flow from the apex of the thermal sensor), Q_h the heating power generated by the probe heater, R_h is the thermal resistance for heat flow through the thermal sensor, R_t is the additional thermal resistance of the NW, $R_{t\text{-}s}$ is the thermal resistance of the interface (contact resistance) between NW and sample, R_s is the spreading thermal resistance of heat flow to the sample from the heater, R_m the thermal resistance of the heat flow to the environment from the thermal sensor apex and T_0 is the ambient temperature.

The heat flow to the sample in zone II can be expressed as a function of these thermal resistances

$$\frac{Q_{hII}}{T_h - T_0} = \frac{1}{R_m} + \frac{1}{R_h + R_t + R_{t-s} + R_s} \tag{1}$$

where T_h is the measurement temperature when the thermal sensor is in contact with the sample and Q_{hII} – heat through zone II. It is clear from equation (1) that decreasing the thermal resistance between thermal sensor and NW as well as contact resistances, whereas increasing the resistance to the environment, improves the sensitivity of SThM to the samples of wider thermal conductivities range. Therefore, NW and contact resistances [20, 27] must be reduced as much as possible to increase the precision of the SThM measurements.

In conventional SThM, several factors can reduce the quality of the measurements. The spatial resolution of the probe depends on the size of the contact area between tip and sample, and especially the heating area when the SThM probe is in contact with a substrate. For instance, the relatively large dimension of the tip (with a typical radius of curvature of 50 to 100 nm) would lead to a low spatial resolution. In addition, interface heat transport effects,

such as Kapitza resistance of the interface [28, 29] due to a contact between two materials can deteriorate the SThM performance. Finally, the influence of environment could change the effective area of contact between tip and sample [24], as well as increase the heat loss to the environment. This work analyzes the contribution of all these factors to the sensitivity of SThM measurements.

In order to analyze the relative contribution of such factors, we developed a simplified analytical model of key components of the SThM cantilever (zone II) with a varying geometry for the NW. The model includes an intermediate layer heater and NW, sample and NW-sample contact resistance. This model was used to investigate the influence of the probe geometry on the thermal properties of the SThM measurements system. Fig. 3 depicts two types of generic geometries where "*contact"* refers to the NW attached to the cantilever apex represented by a cylinder of length L_c. The second type – "*embedded"* where the NW attached to the cantilever apex over the length L_c. These two geometries correspond to different methods of SThM probe fabrication. In the *"contact"* type, the NW probe is directly grown at the tip of cantilever [5, 30], see corresponding schematic in Fig.3a. In turn, the "*embedded"* mode refers to the NW probe attached to the cantilever tip (via the Si_3N_4 layer) using a platinum layer deposited by focused ion beam [22], illustrated in Fig.3b where the NW probe is embedded into the cantilever material. These two manufacturing approaches produce different probes with dissimilar profiles of the thermal sensitivity.

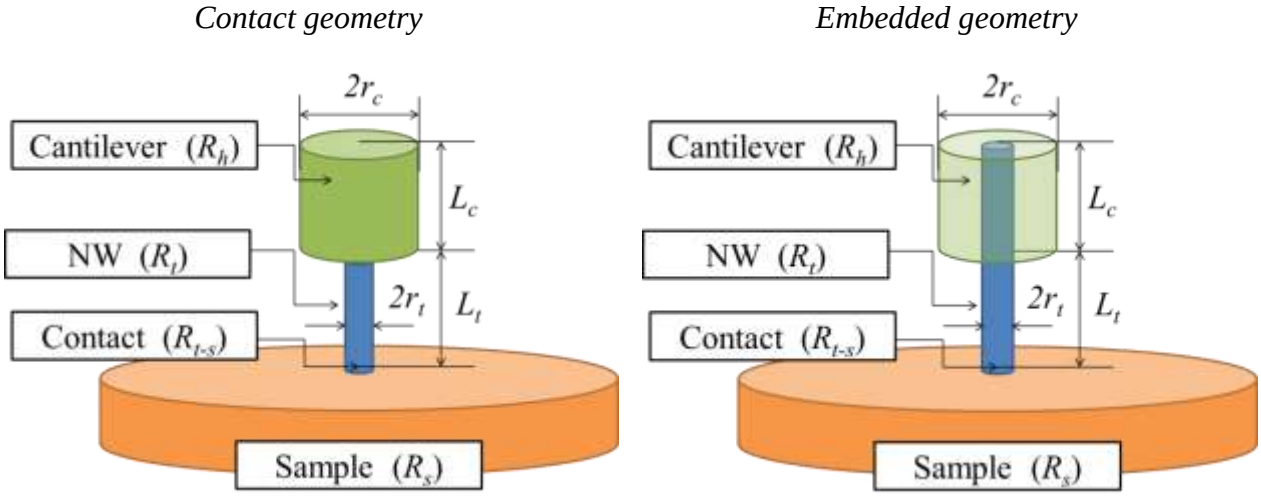

Fig. 3. Schematic diagram of typical NW SThM geometries: (a) *contact* geometry-the NW is contact with cantilever and rests on the top; and (b) *embedded* geometry- the NW is embedded into the cantilever.

While the "*embedded*" geometry is more challenging experimentally, it offers a better prospect of producing a lower thermal resistance between the heater and the probe by virtue

of the increased overlap between the length of the NW probe and the thermal sensor which leads to an enhanced thermal coupling. In "*contact*" geometry, the thermal resistance between the end part of the cantilever and the NW, R_h, is a function of k_c – thermal conductivity of the cantilever material and contact area between cantilever and NW which is dependent on the NW radius r_t. Assuming that the thermal conductivity of the cantilever material is much lower than that of the NW, the thermal resistance R_h in the "*contact"* tip geometry can be expressed using published data, *eq.17* from reference [24], see *eq. 2a*.

$$R_h = \frac{1}{2\pi k_c r_t} \tag{2a}$$

In the *embedded* tip geometry (Fig. 3b), it is assumed that the heater surrounds the tip and the heat flows normally across the sidewalls, through the high thermal conductivity platinum layer. Hence, under this configuration, the thermal resistance can be approximated by that of a cylinder where r_c is the outer radius and r_t the inner radius which is equal to the radius of the NW tip [31].

$$R_h = \frac{\ln\left(r_c / r_t\right)}{2\pi k_c L_c} \tag{2b}$$

The thermal resistance of the cylindrical NW itself can be derived from [31].

$$R_t = \frac{L_t}{\pi k_t r_t^2} \tag{3}$$

L_t and k_t are the length and the thermal conductivity of the NW material, respectively. The thermal conductivity in bulk material and that of the material in NWs geometry can differ significantly depending on the ratio of the mean-free-path of the heat carriers to the dimension of the NW and the scattering of the phonons at the NW surface [32-34]. Here, we consider the thermal conductivity k_t as a three component parameter (k_{tz}, $k_{ty} \approx k_{tx}$) which represents the effective thermal conductivities of the NW, where k_{tz}, the axial component can differ significantly from the radial components.

Thermal contact resistance also known as Kapitza resistance [28, 29] is the resistance due to the presence of an interface between two dissimilar materials. This interfacial thermal resistance plays a significant role in thermal transport at nanoscale measurements [35]. In addition, when the size of the contact approaches the length of the mean free path of the energy carriers (phonons or electrons that can range from a few nm in amorphous oxides to a

few tens of nm in metals and hundreds of nm in Si and graphene) this interfacial thermal resistance in such a ballistic regime can further limit the transport energy in nanostructures as reported elsewhere [36-38]. These may become essential if the length scale of the SThM component decreased further. However, this is beyond the scope of this paper. Kapitza resistance could be presented in *eq.4* to reflect the fact that the contact component of thermal resistance depends on the materials properties and the contact area.

$$R_{t-s} = \frac{\rho_{t-s}}{\pi r_{t-s}^{2}} \tag{4}$$

Here, ρ_{t-s} is the thermal contact resistivity which, in this approximation of the contact between non-metallic materials, depends on the ratio of the Debye temperatures [39] and $r_{t\text{-}s}$ the effective radius (that may be larger than the NW radius). It should be noted, that for high thermal conductivity materials, the effective radius is close to the contact radius since the thermal transport via the surrounding air contributes less to the total heat flux.

For high conductivity materials, such as CNT contacting Al, the effective radius rt-s is very close to rt (where r_t is the radius of the CNT tip). This is particularly helpful as it is these materials where increased mean-free path of heat carriers compared to the contact radius may lead to the square dependence of Kapitza resistance as in Eq. 4. At the same time, for low conductivity materials, a comparison between analytical calculations (where, a simplified estimation rt-s was used) and FEA simulations (with no simplification), suggested no significant difference between in the calculations for high conductivity materials. Therefore, the difference between rt-s and rt can be neglected.

It is well known that different physical mechanisms may contribute to the heat transfer between a SThM cantilever and the sample studied. In addition to the solid-solid heat transfer discussed in this paper, heat conduction through the water meniscus that formed in the contact area between cantilever and the sample [24] should not be discounted, albeit not explicitly included in this work. As demonstrated in the literature [24], the thermal resistance of the water bridge for a typical SThM probe is usually close to 4×10^{5} K W^{-1}, i.e. two orders of magnitude smaller than the thermal resistances described in here. Due to the high aspect ratio of the CNT, the through-the-air conduction has also significantly smaller effect [22] compared to the relatively blunt non-NW probes. Furthermore, due to the very low temperature differences used in the SThM measurements setup considered in this paper, the transfer by thermal radiation between the NW and sample is even less significant and, quantitatively

estimated below in Eqs.7-11 [24]. Finally, the spreading thermal resistance of the sample can be expressed in the form of *eq.5* [24].

$$R_s = \frac{1}{2\pi k_s r_{t-s}} \tag{5}$$

Combining all the thermal resistances (*Eqs. 2a-5*), leads to the full thermal resistance ($R_{i\text{-}m\_con}$) for the *"contact"* geometry.

$$R_{i-m\_con} = \frac{1}{2k_c\pi r_t} + \frac{L_t}{\pi k_t r_t^2} + \frac{\rho_{t-s}}{\pi r_{t-s}^2} + \frac{1}{2\pi k_s r_{t-s}} \tag{6a}$$

Using a similar approach for the *"embedded"* tip geometry, the corresponding thermal resistance ($R_{i\text{-}m\_emb}$) is expressed as:

$$R_{i-m\_emb} = \frac{\ln(r_c / r_t)}{2\pi k_c L_c} + \frac{L_t}{\pi k_t r_t^2} + \frac{\rho_{t-s}}{\pi r_{t-s}^2} + \frac{1}{2\pi k_s r_{t-s}} \tag{6b}$$

It should be noted that for very low thermal conductivity materials, such as polymers, the effective $r_{t\text{-}s}$ can increase significantly due to heat conductance through the air. Although not accounted for in this model, this would result in a decrease in the total thermal contact resistance for such materials which may be estimated using FEA calculation as reported in the literature [4].

Here, the main difference is due to heat transfer normal to the NW axis between the heater and the NW via the cantilever thickness [31] in the embedded geometry which produces the logarithmic term in *Eq. 6b*. As shown in the section 4.1, the values of the ratios between the thermal resistances for both geometries considered are compared with the corresponding SThM experimental measurement data. These ratios provide an explicit dependence of the SThM output as a function of the probe geometry (r_t, L_t, L_c) and the thermal properties of the probe and the sample k_c, k_t, and $\rho_{t\text{-}s}$. *Eq. 6a* and *Eq.6b* highlight the trends of this response for various NW-SThM probe configurations. Further detailed discussion is given in section *4.2*.

As mentioned above, heat transfer by thermal radiation between the NW and SThM cantilever could also alter the results of SThM scanning. The thermal conductance (inverse of thermal resistance), may be described by eq.7 [24]:

$$G_{rad} \approx \frac{4\sigma A T^3}{(1/\varepsilon_1 + 1/\varepsilon_2) - 1} \tag{7}$$

where σ is the Stefan-Boltzmann constant ε_1 and ε_2 are the emissivities of the cantilever and substrate surfaces and *A*, the area of the surface which, as shown in fig. 1 consists of two triangular parts at the end of the cantilever with the base $a \approx 10$ μm. This area is then calculated as:

$$A = 2 \times \frac{\sqrt{3}}{4} a^2 \approx 8.66 \times 10^{-12}\ m^2 \tag{8}$$

The upper limit of radiative conductance was estimated assuming that the surfaces are similar to black bodies:

$$G_{rad} = \frac{4\sigma A T^3}{(1/\varepsilon_1 + 1/\varepsilon_2) - 1} \approx 4\sigma A T^3 \tag{9}$$

For T = 300K, σ = 5.67×10^{-8} Wm^{-2}K^{-4} and A = 8.66×10^{-12} m^2, the the thermal conductance due to the radiation is $G_{rad} = 5\times10^{-11}$ - 10^{-10} WK^{-1}. These values are much lower than the thermal conductance in typical SThM experiments [4]. Therefore, it is reasonable to neglect the effects of radiation in our calculations.

2.2 Numerical analysis of SThM measurements

Previous SThM measurements demonstrated that considerable heat loss occurs at the cantilever apex [4, 6, 24-26]. To investigate the influence of the environment on the SThM system sensitivity, two probe geometries similar to those discussed above were considered. Fig. 4a shows the equivalent thermal resistance diagram of the SThM system exploited in the numerical simulations, while Figs. 4b and 4c illustrate the probe geometries which are similar to those of the analytical model depicting zone II of the SThM probe.

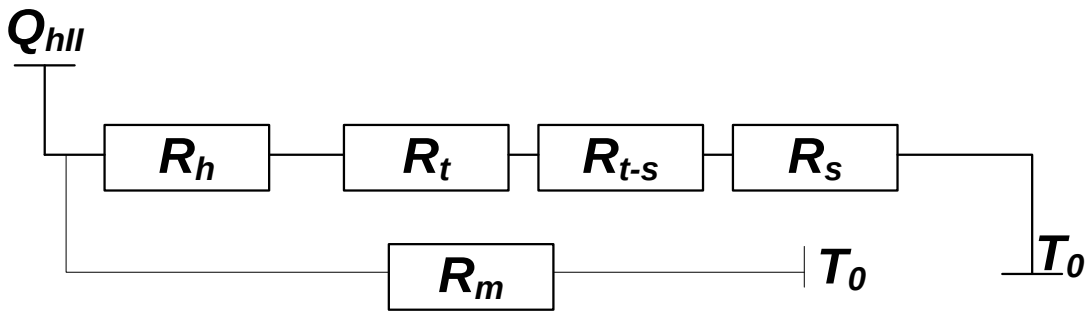

(a)

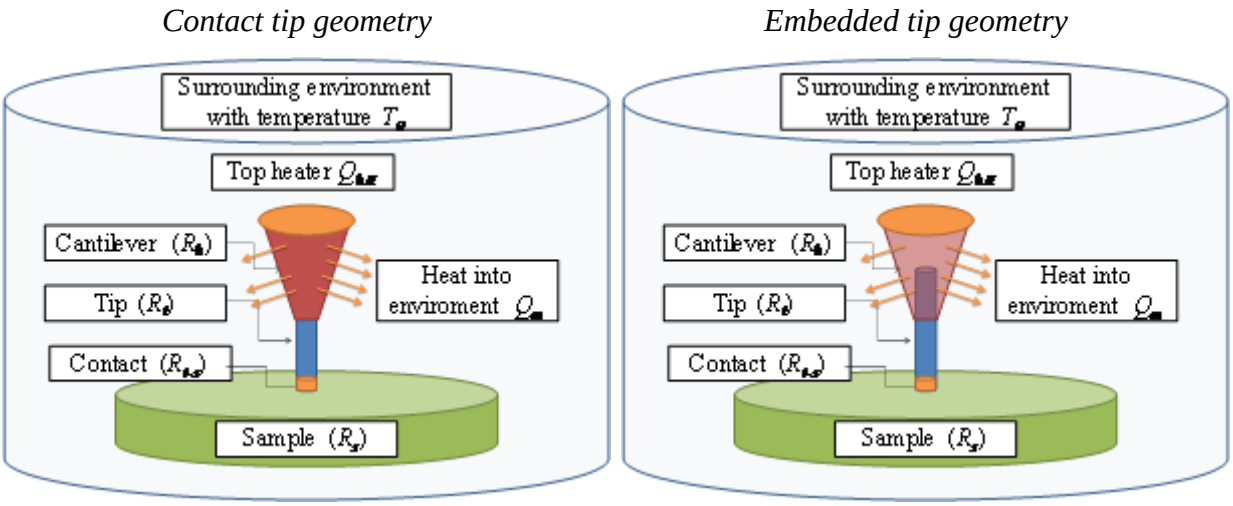

Fig 4. (a) Equivalent thermal resistance diagram for FEA modelling; with *contact* (a) and *embedded* (b) probe-NW geometries.

The modeling geometry has an axial symmetry (as a reasonable approximation reflecting the triangular geometry of the experimental probe) that can represent the main features for the heat flow near the very apex of the tip. Therefore, the heat equation may be presented in cylindrical coordinates r, φ, z where r is the radius, ϕ, the azimuthal angle and z, the coordinate along the probe axis [31].

$$\rho C_p \frac{\partial T}{\partial t} = \frac{1}{r}\frac{\partial}{\partial r}\left(kr\frac{\partial T}{\partial r}\right) + \frac{1}{r^2}\frac{\partial}{\partial \varphi}\left(k\frac{\partial T}{\partial \varphi}\right) + \frac{\partial}{\partial z}\left(k\frac{\partial T}{\partial z}\right) + g(r,\varphi,z,t) \qquad (10)$$

where $T(r,\varphi,z,t)$ is the temperature field, $g(r,\varphi,z,t)$, the density of internal heat generation. ρ, k and C_p are respectively the density, thermal conductivity and heat capacity of the material in the particular domain. The temperature distribution is assumed to be time independent and symmetric around the z axis, without any internal heat generation. Thus, may be simplified Eq. 10 as:

$$0 = \frac{1}{r}\frac{\partial}{\partial r}\left(kr\frac{\partial T}{\partial r}\right) + \frac{\partial}{\partial z}\left(k\frac{\partial T}{\partial z}\right) \qquad (11)$$

For the calculation of the thermal distribution during SThM measurements, the following boundary conditions were used. First, the temperature of the outer limits of surrounding area (see Fig. 4) is fixed:

$$T = T_0 \tag{11a}$$

where T_0 = 300 K. The boundary heat source is placed over the area of the heater (Fig. 4):

$$Q_{hII} = -k\nabla T\big|_{top} \tag{11b}$$

By solving *Eq.11* with the boundary conditions for the shapes considered in the model, one can obtain the temperature distribution in the system including the temperature of the heater T_h. Ultimately, the ratio T_h/Q_{hII} is linked to the thermal resistance of the probe – a parameter measured in SThM. Let us now consider the main heat transfer pathways in this model subsystem, where Q_{hII} is the total heat source, Q_m the heat power lost to the environment and Q_s the heat power transferred to the sample.

$$Q_{hII} = Q_m + Q_s \tag{12}$$

The thermal resistance for SThM probes out of the contact with the sample is given by

$$\frac{Q_{hII}}{T_{nc} - T_0} = \frac{1}{R_m} \tag{13}$$

where T_{nc} the temperature at the top of the tip when the tip is out of contact with sample, T_0 = 300 K is the temperature of the surrounding environment and R_m the thermal resistance of the environment (air, water, dodecane etc.). In contact, Eq. 13 becomes

$$\frac{Q_{hII}}{T_{con} - T_0} = \frac{1}{R_m} + \frac{1}{R_h + R_t + R_{t-s} + R_s} \tag{14}$$

In order to account for the contact resistance in the FEA simulation, we have included in our model a thin resistive layer positioned between the tip apex and the sample with a thickness *h* much smaller than the diameter of the contact. The thermal conductivity of such a layer is calculated as

$$k_{ts} = \frac{h}{R_{t-s}\,\pi\, r_{t-s}^{\,2}} = \frac{h}{\rho_{t-s}} \tag{15}$$

Commercially available finite element analysis (FEA) package (COMSOL Multiphysics) was used to solve stationary heat equations and calculate temperature distributions and the thermal

resistances in our system. Thermal conductivities for materials considered in the model are summarized in the Table 1. [40-43]:

Table 1. Thermal conductivities for materials

Material	**Thermal conductivity, W $m^{-1}K^{-1}$**
Si_3N_4	20
Al	237
Air	0.025
BCB	0.29
MWCNT	1000 (axial direction)

The temperature distributions were found by solving the stationary heat equation (11) for all parts of the described geometries. The boundary conditions for the system were chosen to reflect a typical SThM setup [4]. The surrounding area was thermally anchored at 300 K. The substrate temperature was 300 K while the heater generates a heat flux Q_{hII} on the top of the cantilever.

Temperature distributions were calculated for the *contact* and *embedded* geometries considered (Fig. 4) for a tip length ranging 0 to 1500 nm. The effect of the contact resistance on the heat distribution and materials used was investigated. Fig. 5 illustrates examples of temperature and heat flux distributions in a typical NW-SThM system. In numerical calculations, the SThM probe with a MWCNT tip was used.

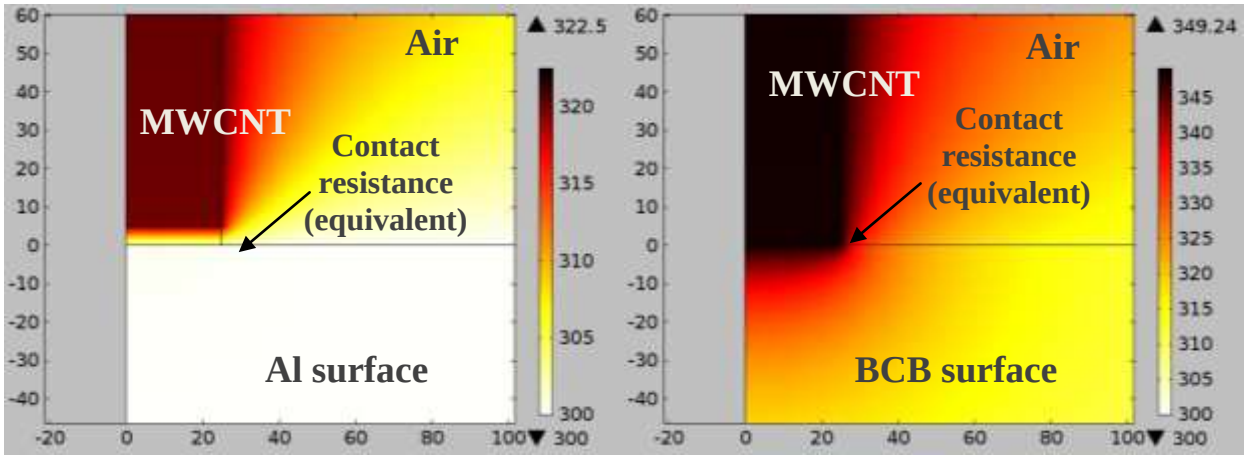

(a) (b)

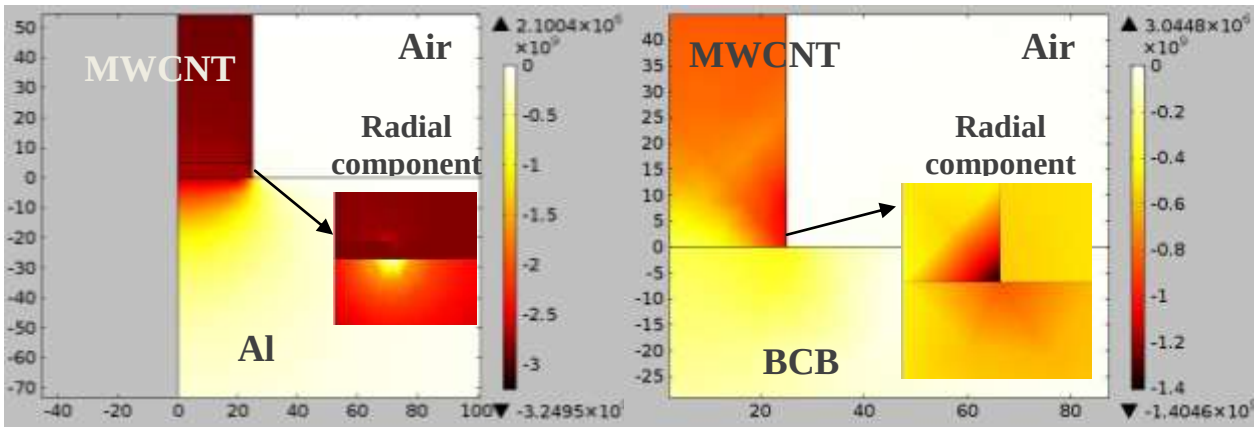

(c) (d)

Fig. 5. Temperature and heat flux distributions in a typical 600 nm MWCNT-SThM system for a Si_3N_4 *embedded* probe, with Al and BCB substrate. (a, b): Cross sectional temperature distribution; (c, d): *z* and *r* components heat flux. The environment was air in all cases.

Fig. 5a-d illustrate the results of FEA modeling of the temperature and heat flux distributions in the NW-SThM system for a 600 nm MWCNT tip embedded in the Si_3N_4 probe and two Al and BCB substrates. These two specimens exhibit quite different thermal conductivities: k_{BCB} = 0.29 $Wm^{-1}K^{-1}$ and k_{Al} =237 $Wm^{-1}K^{-1}$ [42, 43]. Several qualitative features can be drawn from this simulation. According to the heat transfer distribution, the influence of the contact resistance $\rho_{t\text{-}s}$ for the Al sample is much more significant than that of the BCB sample, since the thermal resistance of the BCB sample is much higher compared with the corresponding Kapitza resistance. As demonstrated elsewhere, [39] the thermal boundary resistances between bulk carbon material and polymer materials are close to 10^{-10} K m^2 W^{-1}, i.e. one or two orders of magnitude less than the thermal boundary resistances between carbon materials and metals (10^{-9} – 10^{-8} K m^2 W^{-1}).

For the low thermal conductivity BCB substrate, the heat flux from the cantilever across the ambient increases the effective radius of the thermal contact (Fig. 5d shows that the radial component of the heat transport is notably higher at the perimeter of the NW). In section *4*, the model is applied to determine temperature distributions and thermal resistances for the *contact* and *embedded* geometries and different lengths of MWCNT and GaAs NW-SThM probes (0 -1000 nm). Measurements were taken on Al, BCB, SiO_2 and graphene samples. The model proposed offer the potential to be extended to other material systems.

3. Experimental methods

Standard Si_3N_4 based probes (SThM) with a Pd resistive heater (Kelvin Nanotechnology) were used for measurements [18, 19]. Likewise, similar SThM probes from the same batch

were modified to attach MWCNT tips in order to produce the bespoke MWCNT-SThM probes, using a protocol described elsewhere [22]. Fig. 6 displays a typical SEM image of a MWCNT-SThM probe.

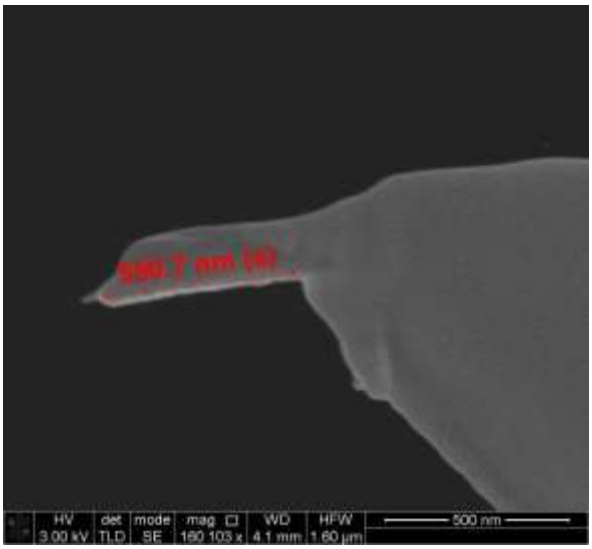

Fig. 6. SEM image of a SThM probe modified with a MWCNT tip (scale bar - 500 nm). The fabrication technique exploiting ion beam milling makes provision to taper the apex of the MWCNT tip such the contact area are may be controlled to a degree.

Further details of the SThM probe calibration and measurements are available in our previous work [6, 23]. In brief, a controlled Joule heating power was applied to the probe, with probe temperature measured immediately before (T_{nc}) and immediately after (T_{con}) solid-solid contact with the material analyzed. This enables the calculation of the probe's thermal contact resistance. In fact, the probe is included in an electric Wheatstone bridge that is balanced before the measurements. The resistance-*vs*-temperature response of the MWCNT-SThM probes was calibrated at 7 temperature points between 20 and 80 ºC by thermal contact of the whole sensor with a Peltier hot/cold plate. The calibration allowed us to correlate the probe's electrical resistance values to the probe heater's temperature T_h. Finally, a lock-in amplifier was used to measure precisely the probe's resistance as a differential signal from the Wheatstone bridge with a sensitivity of the order of 10-20 mK. SThM imaging was performed in a standard SPM setup (Bruker Multimode, 100 mm scanner, Nanoscope IIIa controller, signal access module for readout of external signals) using a SThM probe adapter (Anasys Instruments). The applied DC offset was kept constant during the imaging. In this configuration, the increased heat transport to the sample (due to the local higher thermal conductivity) results in a lower probe temperature [22] for the Al-BCB and graphene – SiO_2

interfaces studied. It should be noted that the MWCNT-SThM probes were robust and able to undergo continuous scanning without damaging the tip.

The Al-BCB ultra large scale integrated polymer interconnects sample [44] was cleaned by sonication in acetone, isopropanol and deionized water, each for 10 minutes, with a final short Ar/O_2 plasma clean. Given the low ability to discriminate between high thermal conductivity samples of is and one of the ongoing challenges for standard SThM probes, graphene on a 280 nm thick SiO_2 was used to test the MWCNT-SThM response to highly conductive materials while ensuring a distinctive thermal contrast between graphene and the SiO_2 substrate. This is because graphene is one of the highest known thermal conductivities in nature (2000-5000 $Wm^{-1}K^{-1}$) [45, 46] while SiO_2 is comparatively a poor thermal conductor. Prior to graphene deposition, the SiO_2/Si substrates were cleaned using a process similar to that described for the Al-BCB sample. Graphene (3 nm thick flakes) was deposited on the 280 nm thick SiO_2/ Si by mechanical exfoliation using a pressure sensitive tape [45].

4. Results and discussion.

4.1 Comparison of FEA simulation with experimental results.

The experimental investigation explored Al-BCB and graphene on Si/SiO_2 samples which exhibit different thermal properties. SThM scanning was conducted normal to the surface to extract topographical and the thermal profiles of the specimens investigated. The sensitivity of SThM is given by the ratio between the thermal resistances for two different materials, e.g. Al to BCB or SiO_2 to graphene. For comparison, a standard SThM and MWCNT-SThM probes were utilized to conduct the experiments and modelled in the FE simulations.

In line with the generalized SThM model (Fig. 2 and Fig. 4(a)), the thermal resistance of the cantilever and tip is given by

$$\frac{Q_{hII}}{\left(T_{con-i}-T_0\right)}-\frac{Q_{hII}}{\left(T_{nc-i}-T_0\right)}=\frac{Q_{hII}\left(T_{nc-i}-T_{con-i}\right)}{\left(T_{con-i}-T_0\right)\left(T_{nc-i}-T_0\right)}=\frac{1}{R_h+R_t+R_{t-s}+R_s}=\frac{1}{R_i} \qquad (16)$$

where T_{con-i} and T_{nc-i} are the temperatures of the probe in-contact and out-of-contact with sample *i* (Al, BCB, SiO_2 or graphene). R_i is defined as the thermal resistance of the probe in contact with material *i*. R_0 is the overall thermal resistance of the *zone I* of SThM probe (Figs. 1, 2) that includes heat flow to the cantilever base and thermal losses to the environment.

$$\frac{1}{R_0} = \frac{1}{R_{mfull}} + \frac{1}{R_c} \tag{17}$$

The experimentally measured thermal resistance of the probe in contact with sample *i* or *j* is given by

$$\frac{1}{R_{i,j-m}} = \frac{1}{R_0} + \frac{1}{R_{i,j}} \tag{18}$$

Using this description, one can compare the experimental values of the thermal resistance ratios R_{i-m} / R_{j-m}, namely, R_{Al-m} / R_{BCB-m} and R_{GR-m} / R_{SiO2-m} in structures like Al-BCB and graphene-on-SiO_2.

Given the Kapitza resistance at the tip and substrate interface affects significantly SThM measurements [27, 36, 39, 47], it must be considered to achieve a realistic model of SThM measurements. Literature estimates of Kapitza resistance values vary significantly and are not always available for the particular materials studied. Therefore, thermal resistances reported elsewhere [39] were used for different interfaces to select pairs of materials which exhibit similar thermal properties, e.g. polymer and metals to match the SThM probe and the sample material. As discussed in section 2, the thermal contact resistance of BCB neglected due to the high thermal resistance of the polymer itself. For other pairs, the values were selected according to similarity of speed of sound in the materials (acoustic phonons) and their Debye temperature data (θ_D). In the modelling Si_3N_4 ($\theta_D \approx 923$ K) [48] was replaced by magnesium oxide (MgO) with ($\theta_D \approx 941$ K) [39] and SiO_2 with ($\theta_D \approx 470$ K) [39]. MWCNT and graphene were extrapolated to diamond with $\theta_D = 1860$ K [39]. For Al surface, $\theta_D = 394$ K [39]. These values allowed us to estimate contact resistances for numerical calculations, in line with to published data [39] for C-Al interface $\rho_{C\text{-}Al} = 9\times10^{-9}$ Km^2W^{-1} and Si_3N_4-Al $\rho_{Si3N4\text{-}Al} = 4.5\times10^{-9}$ Km^2W^{-1}.

Fig. 7 compares the experimental SThM results of $1-R_{i-m} / R_{j-m}$ for Al-BCB structures to that of modelling of this ratio which depend on the thermal contact resistance value ($\rho_{t\text{-}s}$). Green and red bands describe the ranges of experimental data (ratio between measured thermal resistances for BCB and Al substrates) while the data points correspond to the calculated results.

The simulation was carried out using the models presented in the Fig. 4 for a cantilever with a conical shape at the apex. The MWCNT was 1000 nm long of which, 500 nm was embedded

into the cantilever, leaving a 500 nm long MWCNT tip with a conical shape (500 nm radius at the base and 25 nm tip radius). Thermal conductivity of 1000 and 230 $Wm^{-1}K^{-1}$ [2] were considered for MWCNT and Al, respectively. The ambient temperature T_0 = 300 K, Q_h was selected such that $T_{nc} \approx$ 360 K, were also utilized, albeit Q_h does not influence directly the thermal resistances measured.

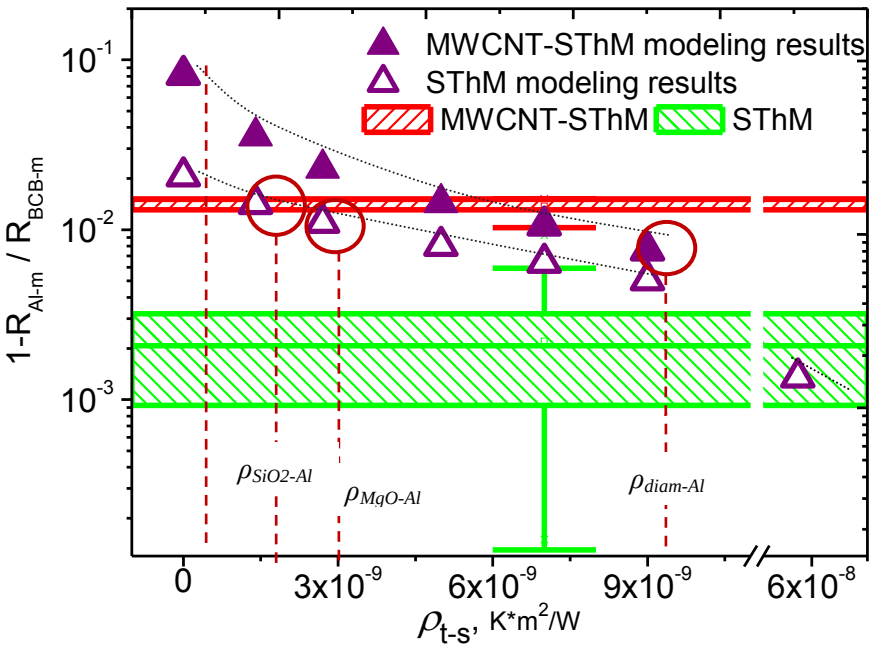

Fig. 7. Results of Al and BCB thermal resistances ratios ($1-R_{Al-m} / R_{BCB-m}$) measured Experimentally. Green and red bands are the experimental SThM measurements for standard Si_3N_4 SThM and CNT-SThM probes, respectively. The error band for the experimental measurements for the MWCNT-SThM (red bar) is dominated by the statistical error of the repeated measurements, whereas for the standard SThM probe it is dominated by the noise of the temperature measurements. Triangles: modelling results for different thermal contact resistances (horizontal axis). Open and solid triangles correspond to standard SThM MWCNT-SThM probes, respectively. the red circles are the literature data [39] for contact resistances.

In general, higher ratios are indicative of a superior SThM performance. It is clear from Fig. 7 that CNT-SThM probes improve significantly the sensitivity of the SThM system [4]. For different contact resistance values, Fig. 7 also shows a good correlation between experimental and FEA modelling results. These data were utilized to extract, direct estimates of contact thermal resistances measured experimentally for various interfaces: MWCNT-Al (ρ_{t-s} = $5\times10^{-9} \pm 1\times10^{-9}$ K m^2 W^{-1}), and Si_3N_4-Al (ρ_{t-s} = $6\times10^{-8} \pm 2.5\times10^{-8}$ K m^2 W^{-1}). Interestingly, the thermal contact resistance measured between MWCNT-Al is lower than that between diamond and Al [39] of ~1×10^{-8} K m^2 W^{-1}. This is may be attributable to the fact that MWCNT has a lower Debye temperature compared with perfect diamond and the possible

influence of thermal transport anisotropy of MWCNT. These results also suggest a relatively perfect contact between MWCNT and Al (not leading to any excess contact resistance). In contrast, the thermal resistance between a standard Si_3N_4 SThM probe and Al is significantly higher than suggested by the literature (by an order of magnitude), suggesting that the contact between these materials may have a multi-asperity nature [49] that can significantly degrade the contact and increase the contact resistance, as a result.

The results of a similar investigation of graphene on SiO_2/Si substrates are compiled in Fig.8, where the experimental results of the $1-R_{GR-m}/R_{SiO2-m}$ ratio between graphene flakes and SiO_2/Si are compared with the results of modelling. These data indicate that the experimental sensitivity of the standard Si_3N_4 SThM is similar to that of the MWCNT-SThM probe. This suggests that the MWCNT-SThM probe is not significantly better for measuring the absolute values of thermal conductivity for the graphene-SiO_2/Si matrix. However, the spread of experimental results for MWCNT-SThM tips is much smaller than that of the Si_3N_4 SThM probe, which is highly desirable. The similarity observed is perhaps also due to the fact the contact resistance values were based on literature data for interfaces between similar materials, but somewhat different from that of the materials used – 7.3×10^{-10} and 7.5×10^{-10} K m^2 W^{-1} [39]. In addition, the ratios measured experimentally in this work are significantly lower than predicted by FEA, in the absence of the contact resistance. Comparison between experiment and calculations shows that the contact resistance will be significantly larger (close to 10^{-8} K m^2 W^{-1}) for MWCNT-graphene and Si_3N_4-graphene interfaces. This strongly suggests that there are other mechanisms leading to the increased contact resistance. These may include multi-asperity contacts, large anisotropy of graphene in plane and normal to the graphene planes direction and the likely effects of the ballistic thermal conductance due to the large mean-free-path in both MWCNT and graphene layer [37].

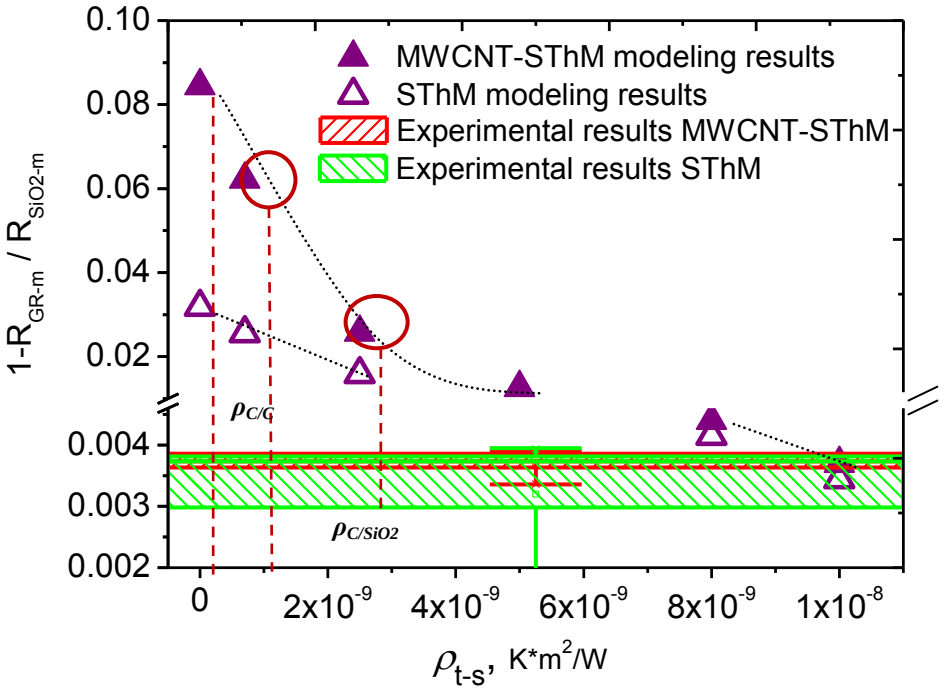

Fig. 8. Thermal resistance ratio ($1-R_{GR-m}/R_{SiO2-m}$) of graphene and SiO_2/Si substrates. Green and red bands are the experimental SThM measurements for standard Si_3N_4 SThM and CNT-SThM probes, respectively. Triangles: modelling results for different thermal contact resistances (horizontal axis). Open and solid triangles correspond to standard SThM MWCNT-SThM probes, respectively. the red circles are the literature data [39] for contact resistances.

4.2 Comparison of analytical and FEA modelling results

The analytical model developed for the SThM cantilever facilitates the analysis of the relative contribution for the various parameters affecting the SThM performance. This model describes how the cantilever geometry, tip length, radius, tip material and substrate influence the sensitivity of the SThM probes. Fig. 9 compares the thermal resistance R_i for the *contact* ($R_{i\text{-}m\_con}$, *eq. 6a*) and *embedded* ($R_{i\text{-}m\_emb}$, *eq. 6b)* geometries described in Fig. 3 & 4. The values of R_i (*eq. 16*) were obtained by numerical calculations for different typical radii (12.5, 25 and 50 nm) of the embedded and contact *NWs*. Fig. 9 also displays the dependence of the thermal resistance on the probe tip geometry. Lines correspond to the analytical model while solid data points depict the numerical FEA modeling results. Note that the parameters for the numerical and analytical calculations are identical to those described in section *4.1*.

Embedded geometry

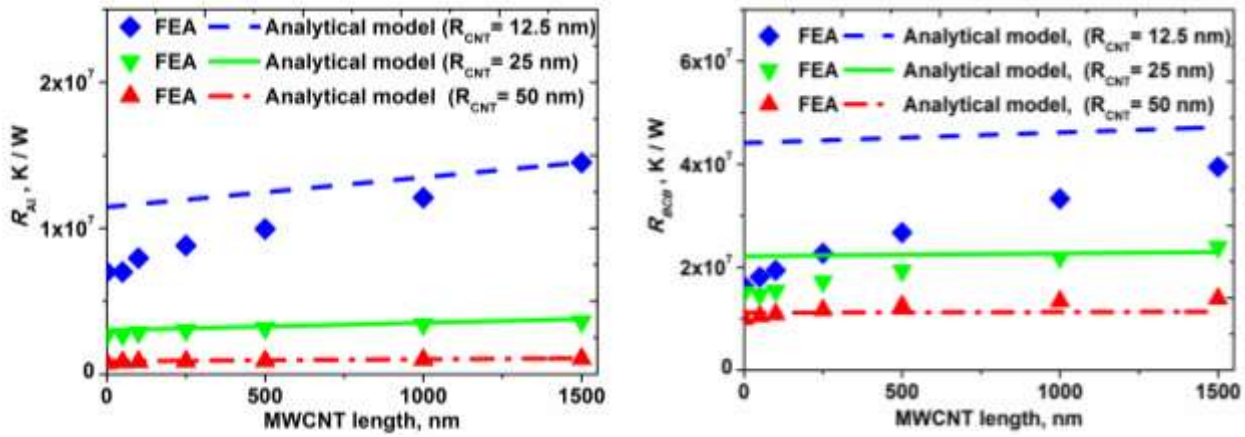

Fig. 9. Comparison of FEA modeling (solid data points) and analytical estimates (lines) of the sample thermal resistance R_i as a function of the MWCNT length and radius (R_{CNT}) for the *embedded* probe geometry. R_{Al} and R_{BCB} are the thermal resistances for the Al (a) and BCB (b) investigated, respectively. Note a good correlation between the analytical and FE model results for the Al, and for both Al and BCB for the larger diameter of the NW. While most significant deviation between these models occurs for the high thermal conductivity material and short NW, the values for Al are still within 0-40%, suggesting that analytical models can be used for a semi-quantitative prediction of performance of NW probes in SThM for such materials. Clearly, the effects of the water meniscus and the through–the-air conductance for the shorter NW should be taken into account for the ambient environment SThM, while the model would still remain valid for vacuum SThM measurements.

Results for the Al substrate shown in Fig. 9a, b show a good agreement between numerical and analytical calculations. The differences observed in R_i for the analytical and numerical models for BCB substrates, especially for small length of MWCNT, can be explained by an increase in the effective radius of heating in comparison with the actual contact radius between the MWCNT tip and the BCB substrate due to conductance through air (see Fig. 5).

Finally, Fig. 10 compares the calculated SThM sensitivities for MWCNT and GaAs NW for different length of the MWCNT and NW tip. The thermal conductivity of GaAs NW was 30 W m^{-1} K^{-1}[50].

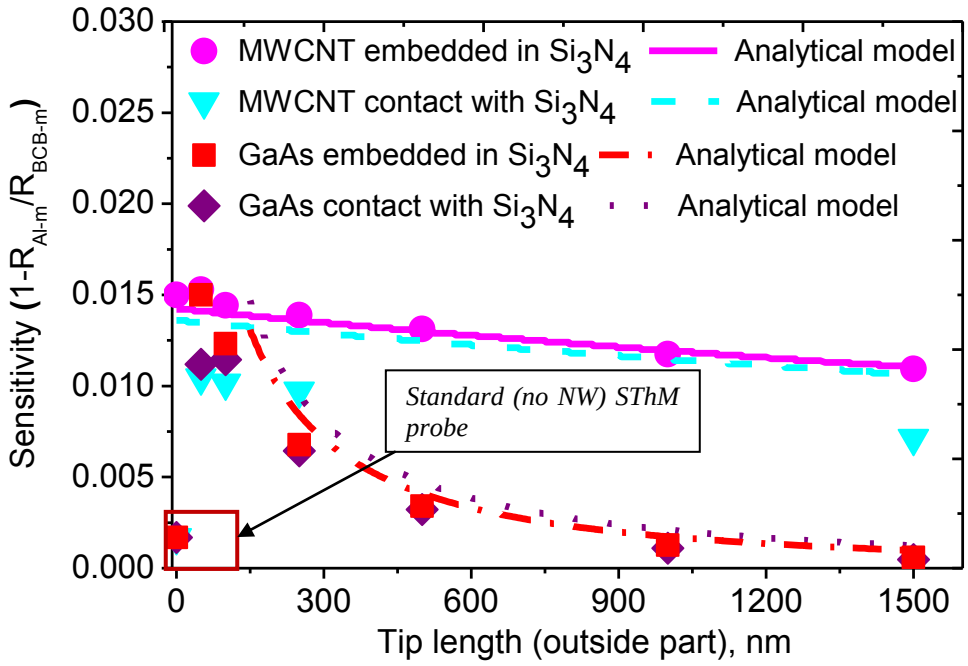

Fig. 10. Dependence of the SThM sensitivity on the tip length for MWCNT and GaAs tips. data points correspond to FEA calculations while lines represent the analytical model.

The analysis of the results presented in Fig. 10 indicates that the modification of SThM probes with high thermal conductivity MWCNT does increase the sensitivity of SThM, regardless of the MWCNT lengths considered. Other NW tips – such as semiconducting GaAs can also improve the sensitivity of the SThM, providing the NW tip is relatively short (below 100-200 nm). These findings, i.e., the possibility of effective use of III-V semiconducting NWs, may extend SThM functionality to electrical field or current sensing probes.

5. Conclusions

A simple analytical model of SThM with a thermally conductive NW probe was developed to elucidate the key phenomena affecting SThM measurements of low and high thermal conductivity materials. These include effects of NW thermal conductivity, the geometry of the probe and the NW and the effects of the contact resistance. The combination of the analytical model, FEA modelling of standard SThM and NW-SThM probes and the comparison between analytical, FEA and experimental data allowed us to provide direct estimates of the thermal contact resistances for interfaces such as MWCNT-Al ($5\times10^{-9} \pm 1\times10^{-9}$ W m^{-1} K^{-1}), Si_3N_4–Al ($6\times10^{-8} \pm 2.5\times10^{-8}$ W m^{-1} K^{-1}) and Si_3N_4–graphene (10^{-8} W m^{-1} K^{-1}). These results suggest that a multi-asperity nature of the contact and anisotropy of the MWCNT may significantly influence the contact resistance. The analysis has also indicated that these models may be efficiently used for NWs with a radius of 25 nm and above to provide

significant tools for the development of novel SThM probes that include semiconductor NWs which, in turn, can enable additional functionalities in SThM measurement.

5. Acknowledgments

Authors acknowledge useful discussion with Vladimir I. Falko from Lancaster University regarding the nature of nanoscale transport and physical interpretation of the thermal models. Authors also acknowledge input of Craig Prater and Roshan Shetty from Anasys Instruments for the support related to the SThM development. We also acknowledge Dr MC Rosamond, formerly at Durham University, for his assistance in the fabrication MWCNT probes. We acknowledge the support from the EPSRC grants EP/G015570/1 and EP/G017301/1, EP/K023373/1, and EU FP7 grants, QUANTIHEAT (GA-604668), FUNPROB (GA-269169) and NanoEmbrace (GA-316751), Royal Academy of Engineering/The Leverhulme. M Timofeeva and V. G. Dubrovskii gratefully acknowledge financial support of support Russian Science Foundation (project No. 14-22-00018).

References

[1] K. Luo, M. Lederman, A. Majumdar, Liquid-film-mediated scanning thermal microscopy of a magnetoresistive reading head, Microscale Thermophysical Engineering, 1 (1997) 333-345.
[2] A.A. Balandin, Thermal properties of graphene and nanostructured carbon materials, Nat. Mater., 10 (2011) 569-581.
[3] W. Cai, A.L. Moore, Y. Zhu, X. Li, S. Chen, L. Shi, R.S. Ruoff, Thermal transport in suspended and supported monolayer graphene grown by chemical vapor deposition, Nano Lett, 10 (2010) 1645-1651.
[4] P. Tovee, M.E. Pumarol, D.A. Zeze, K. Kjoller, O. Kolosov, Nanoscale spatial resolution probes for Scanning Thermal Microscopy of solid state materials, J. Appl. Phys., 112 (2012) 114317.
[5] M.A. Lantz, B. Gotsmann, U.T. Durig, P. Vettiger, Y. Nakayama, T. Shimizu, H. Tokumoto, Carbon nanotube tips for thermomechanical data storage, Applied Physics Letters, 83 (2003) 1266-1268.
[6] M.E. Pumarol, M.C. Rosamond, P. Tovee, M.C. Petty, D.A. Zeze, V. Falko, O.V. Kolosov, Direct Nanoscale Imaging of Ballistic and Diffusive Thermal Transport in Graphene Nanostructures, Nano Letters, 12 (6) (2012) 2906–2911.
[7] G.E. Moore, Cramming more components onto integrated circuits, Electronics, 38 (1965) 114-117.
[8] S. Borkar, Design challenges of technology scaling, IEEE Micro, 19 (1999) 23-29.
[9] D.J. Frank, Power-constrained CMOS scaling limits, IBM J. Res. Develop, 46 (2002) 235-244.
[10] A. Soudi, R.D. Dawson, Y. Gu, Quantitative Heat Dissipation Characteristics in Current-Carrying GaN Nanowires Probed by Combining Scanning Thermal Microscopy and Spatially Resolved Raman Spectroscopy, Acs Nano, 5 (2011) 255-262.
[11] K. Kim, J. Chung, G. Hwang, O. Kwon, J.S. Lee, Quantitative Measurement with Scanning Thermal Microscope by Preventing the Distortion Due to the Heat Transfer through the Air, Acs Nano, 5 (2011) 8700-8709.
[12] K. Kim, W.H. Jeong, W.C. Lee, P. Reddy, Ultra-High Vacuum Scanning Thermal Microscopy for Nanometer Resolution Quantitative Thermometry, Acs Nano, 6 (2012) 4248-4257.
[13] E. Puyoo, S. Grauby, J.M. Rampnoux, E. Rouviere, S. Dilhaire, Thermal exchange radius measurement: Application to nanowire thermal imaging, Review of Scientific Instruments, 81 (2010).
[14] J. Duvigneau, H. Schonherr, G.J. Vancso, Nanoscale Thermal AFM of Polymers: Transient Heat Flow Effects, Acs Nano, 4 (2010) 6932-6940.
[15] P.G. Klemens, Theory of thermal conduction in thin ceramic films, Int. J. Thermophys., 22 (2001) 265-275.
[16] J. Chung, K. Kim, G. Hwang, O. Kwon, S. Jung, J. Lee, J.W. Lee, G.T. Kim, Quantitative temperature measurement of an electrically heated carbon nanotube using the null-point method, Rev Sci Instrum, 81 (2010) 114901.
[17] E. Gmelin, R. Fischer, R. Stitzinger, Sub-micrometer thermal physics - An overview on SThM techniques, Thermochim. Acta, 310 (1998) 1-17.
[18] http://www.windsorscientific.co.uk/KNT-SThM-1an-datasheet.pdf. [updated © 2015 - Windsor Scientific].
[19] http://www.nanoandmore.com/AFM-Probe-KNT-SThM-1an.html. [updated ® 2012 NanoAndMore].

[20] T.Z. Jeong , J. G.; Chung S.; Gibbons M. R. , Thermal boundary resistance for gold and CoFe alloy on silicon nitride films, J. Appl. Phys., 111 (2012) 083510.
[21] J. Hirotani, J. Amano, T. Ikuta, T. Nishiyama, K. Takahashi, Carbon nanotube thermal probe for quantitative temperature sensing, Sensors and Actuators A: Physical, 199 (2013) 1-7.
[22] P.D. Tovee, M.E. Pumarol, M.C. Rosamond, R. Jones, M.C. Petty, D.A. Zeze, O.V. Kolosov, Nanoscale resolution scanning thermal microscopy using carbon nanotube tipped thermal probes, Physical Chemistry Chemical Physics, 16 (2014) 1174-1181.
[23] P. Tovee, D., O. Kolosov, V., Mapping nanoscale thermal transfer in-liquid environment—immersion scanning thermal microscopy, Nanotechnology, 24 (2013) 465706.
[24] A. Majumdar, Scanning thermal microscopy, Annu. Rev. Mater. Sci., 29 (1999) 505-585.
[25] N.V.S. Sibirev, I. P.;Dubrovskii, V. G.;Arshansky E. B., Temperature profile along a nanowhisker growing in high vacuum, Technical Physics Letters, 32 (2006) 292-295.
[26] A.T.F. Galisultanov, I. A.; Sibirev, N. V.; Soshnikov, I. P.; Dubrovskii, V. G.;, Effect of growth atmosphere on the temperature profile along a nanowhisker, Technical Physics Letters, 34 (2008) 512-515.
[27] J. Hirotani, T. Ikuta, T. Nishiyama, K. Takahashi, Thermal boundary resistance between the end of an individual carbon nanotube and a Au surface, Nanotechnology, 22 (2011) 315702.
[28] R.E.A. Peterson, A. C.; , The Kapitza thermal boundary resistance, Journal of Low Temperature Physics, 11 (1973) 639-665.
[29] G. Balasubramanian, I.K. Puri, Heat conduction across a solid-solid interface: Understanding nanoscale interfacial effects on thermal resistance, Applied Physics Letters, 99 (2011).
[30] J.P. Edgeworth, D.P. Burt, P.S. Dobson, J.M.R. Weaver, J.V. Macpherson, Growth and morphology control of carbon nanotubes at the apexes of pyramidal silicon tips, Nanotechnology, 21 (2010) 105605-105615.
[31] J.H. Lienhard, A Heat Transfer Textbook, Phlogiston Press, Cambridge, Massachusett, 2008.
[32] I.Z. M. Soini, E. Uccelli, S. Funk, G. Koblmüller, A. Fontcuberta i Morral, G. Abstreiter, Thermal conductivity of GaAs nanowires studied by micro-Raman spectroscopy combined with laser heating, Applied Physics Letters, 97 (2010) 263107.
[33] S. Grauby, E. Puyoo, J.-M. Rampnoux, E. Rouvière, S. Dilhaire, Si and SiGe Nanowires: Fabrication Process and Thermal Conductivity Measurement by 3ω-Scanning Thermal Microscopy, The Journal of Physical Chemistry C, 117 (2013) 9025-9034.
[34] N. Mingo, Calculation of Si nanowire thermal conductivity using complete phonon dispersion relations, Physical Review B, 68 (2003) 113308.
[35] D.G. Cahill, W.K. Ford, K.E. Goodson, G.D. Mahan, A. Majumdar, H.J. Maris, R. Merlin, Phillpot, Sr., Nanoscale thermal transport, Journal of Applied Physics, 93 (2003) 793-818.
[36] R. Prasher, Thermal boundary resistance of nanocomposites, International Journal of Heat and Mass Transfer, 48 (2005) 4942-4952.
[37] R. Prasher, Predicting the thermal resistance of nanosized constrictions, Nano Letters, 5 (2005) 2155-2159.
[38] R.S. Prasher, P.E. Phelan, Microscopic and macroscopic thermal contact resistances of pressed mechanical contacts, Journal of Applied Physics, 100 (2006).
[39] H.X. Wang, Y.; Shimono, M.;Tanaka, Y.;Yamazaki, M.;, Computation of Interfacial Thermal Resistance by Phonon Diffuse Mismatch Model, Materials Transactions, 48 (2007) 2349-2352.
[40] http://www.ceradyne.com/uploads/Brochures/SiN_Brochure.pdf, [updated © 3M 2015]
[41] http://en.wikipedia.org/wiki/List_of_thermal_conductivities, [updated 12.05.2015]
[42] http://pubs.acs.org/subscribe/archive/ci/31/i12/html/12so_box.html.

[43] http://www.nist.gov/data/nsrds/NSRDS-NBS-8.pdf, [issued 25 November 1966]
[44] R.E. Geer, O.V. Kolosov, G.A.D. Briggs, G.S. Shekhawat, Nanometer-scale mechanical imaging of aluminum damascene interconnect structures in a low-dielectric-constant polymer, Journal of Applied Physics, 91 (2002) 4549-4555.
[45] K.S. Novoselov, A.K. Geim, S.V. Morozov, D. Jiang, Y. Zhang, S.V. Dubonos, I.V. Grigorieva, A.A. Firsov, Electric field effect in atomically thin carbon films, Science, 306 (2004) 666-669.
[46] A.A. Balandin, S. Ghosh, W. Bao, I. Calizo, D. Teweldebrhan, F. Miao, C.N. Lau, Superior Thermal Conductivity of Single-Layer Graphene, Nano Letters, 8 (2008) 902-907.
[47] H.L. Zhong, J. R.; , Interfacial thermal resistance between carbon nanotubes: Molecular dynamics simulations and analytical thermal modeling, Phys. Rev. B, 74 (2006) 125403.
[48] S.P.C. Dodd, M.; Saunders, G. A.; James, B., Ultrasonic study of the temperature and pressure dependences of the elastic properties of β-silicon nitride ceramic, Journal of Materials Science, 36 (2001) 2557-2563.
[49] L. Shi, A. Majumdar, Thermal transport mechanisms at nanoscale point contacts, Journal of Heat Transfer-Transactions of the Asme, 124 (2002) 329-337.
[50] I.Z. M. Soini, E. Uccelli, S. Funk, G. Koblmüller, A. Fontcuberta i Morral, G. Abstreiter, Thermal conductivity of GaAs nanowires studied by micro-Raman spectroscopy combined with laser heating, Appl. Phys. Lett., 97 (2010) 263107.